The large-scale orientations of disc galaxies

Author(s):
Hahn, Oliver; Teyssier, Romain; Carollo, C. Marcella

The large-scale orientations of disc galaxies

Oliver Hahn,[1,2]★ Romain Teyssier[3,4] and C. Marcella Carollo[1]

[1]*Department of Physics, ETH Zurich, CH-8093 Zürich, Switzerland*
[2]*KIPAC, Stanford University, 2575 Sand Hill Road, Menlo Park, CA 94025, USA*
[3]*Institute for Theoretical Physics, University of Zurich, CH-8057 Zürich, Switzerland*
[4]*CEA Saclay, DSM/IRFU/SAP, Bâtiment 709, F-91191 Gif-sur-Yvette, Cedex, France*

ABSTRACT

We use a 380-h^{-1} pc resolution hydrodynamic adaptive mesh refinement (AMR) simulation of a cosmic filament to investigate the orientations of a sample of $\sim$100 well-resolved galactic discs spanning two orders of magnitude in both stellar and halo mass. We find: (i) at $z = 0$, there is an almost perfect alignment at a median angle of $18°$, in the inner dark matter halo regions where the discs reside, between the spin vector of the gaseous and stellar galactic discs and that of their inner host haloes. The alignment between galaxy spin and spin of the entire host halo is however significantly weaker, ranging from a median of $\sim46°$ at $z = 1$ to $\sim 50°$ at $z = 0$. (ii) The most massive galaxy discs have spins preferentially aligned so as to point along their host filaments. (iii) The spin of discs in lower mass haloes shows, at redshifts above $z \sim 0.5$ and in regions of low environmental density, a clear signature of alignment with the intermediate principal axis of the large-scale tidal field. This behaviour is consistent with predictions of linear tidal torque theory. This alignment decreases with increasing environmental density, and vanishes in the highest density regions. Non-linear effects in the high-density environments are plausibly responsible for establishing this density-alignment correlation. We expect that our numerical results provide important insights for both understanding intrinsic alignment in weak lensing from the astrophysical perspective and formation and evolution processes of galactic discs in a cosmological context.

Key words: methods: numerical – galaxies: evolution – galaxies: formation – cosmology: theory – large-scale structure of Universe.

1 INTRODUCTION

Numerical simulations and analytic calculations have shown that the gravitational growth of tiny density perturbations in the Λ cold dark matter cosmological model leads to a wealth of structures over cosmic time. The spatial distribution of gravitationally bound structures follows a web-like pattern composed of dense clusters, filaments, sheets and otherwise near-empty void regions (see e.g. Shandarin & Zeldovich 1989; Bond, Kofman & Pogosyan 1996). This 'cosmic web' is the weakly non-linear manifestation of the large-scale tidal field and its formation can be readily understood in the first-order Lagrangian perturbation theory of the Zel'dovich approximation (Zel'dovich 1970). Recent large-scale galaxy surveys have observationally confirmed the presence of the cosmic web in the Universe (e.g. Colless et al. 2001; Tegmark et al. 2004).

Since galaxies form and evolve together with the cosmic web in which they are embedded, it is a question of high relevance whether the properties of galaxies depend on scales beyond the most immediate vicinity and thus reflect the effect of large-scale tidal fields on the assembly of the galaxy. General ellipsoidal density perturbations collapse sequentially along their three axes leading to matter accreting first on to a sheet, then collapsing to a filament before matter finally streams along the filaments into the densest regions. As a consequence of these processes, the large-scale morphology of the cosmic web might leave its imprint on the orientations of galaxies through the anisotropy of accretion and mergers.

Recently, evidence has accumulated that galaxies are indeed not oriented randomly with respect to one another. On small scales, several studies report a radial alignment of satellite galaxies towards the centre of mass of the group or cluster in which they reside (e.g. Zentner et al. 2005; Yang et al. 2006; Agustsson & Brainerd 2006a,b; Azzaro et al. 2007; Faltenbacher et al. 2007, 2008). Such an alignment is predicted by *N*-body simulations of dark matter (DM) haloes (e.g. Bailin & Steinmetz 2005; Knebe et al. 2008; Pereira et al. 2008). It is commonly believed that tidal torques are responsible for this radial alignment (e.g. Ciotti & Dutta 1994; Ciotti & Giampieri 1998; Pereira et al. 2008), as tidal forces on these relatively small scales ($\lesssim$1 Mpc) are sufficiently strong to affect halo shapes on short time-scales.

★E-mail: hahn@phys.ethz.ch

More surprisingly, however, observational results indicate that the orientations of galaxies are correlated up to scales of order ∼100 times larger than the virial radii of their host haloes. Mandelbaum et al. (2006), Okumura, Jing & Li (2009) and Faltenbacher et al. (2009) detect an alignment of galaxy shapes for the luminous red galaxies (LRGs) in the Sloan Digital Sky Survey (SDSS) out to the largest probed scales (∼80 Mpc). Hirata et al. (2007) report a similar result for redshifts $0.4 < z < 0.8$. Bailin et al. (2008) find an alignment of late and intermediate type galaxies in SDSS with the surrounding large-scale structure. For lower luminosity galaxies, in particular for $L < L_*$, no alignment has been detected yet (see also Slosar & White 2009), although some results using N-body simulations indicate shape (Patiri et al. 2006) or spin alignment (Brunino et al. 2007; Cuesta et al. 2008) around voids. Correlations of the spin of galaxies have been the subject of several analytical models (see e.g. Schäfer 2009, for a review, and references therein).

Compared with more local effects, the relative weakness on galaxy scales of tidal forces arising from the ≫1 Mpc scales requires that such effects maintain spatial coherence over rather long time-scales for them to be able to affect galaxy properties. Also it is not clear how they are counteracted by local non-linear effects in the most immediate vicinity of the galaxy: non-linear gravitational effects as well as ram pressure exerted on the disc gas could potentially lead to a reorientation of galactic angular momentum. Furthermore, the impact of hot in contrast to cold mode accretion separated by a halo mass of $\sim 4 \times 10^{11} \, h^{-1} \, M_\odot$ of gas on to galaxies (cf. Birnboim & Dekel 2003; Kereš et al. 2005; Dekel & Birnboim 2006; Ocvirk, Pichon & Teyssier 2008) on the orientation of the resulting discs is not clear.

While understanding the formation of galaxies in the context of their host large-scale structure is a key question for galaxy formation theory, a precise knowledge of correlated galaxy orientations is of high importance also for future high-precision weak lensing studies of dark energy. Weak lensing signals can be severely affected by systematic contaminations due to large-scale alignments in the spatial distribution of cosmic matter on scales from a few to more than a hundred Mpc (due to galaxy ellipticity–ellipticity alignment: Catelan, Kamionkowski & Blandford (2001); and due to the much more problematic shear–ellipticity alignment: Hirata & Seljak (2004). Approaches that have been suggested so far to remove the contamination due to shear–ellipticity alignment suffer from several limitations and uncertainties: the statistical down-weighting of the effect proposed by Joachimi & Schneider (2008) relies on precision determinations of photometric galaxy redshifts; other techniques, such as proposed by e.g. King (2005), depend heavily on toy models (e.g. Catelan et al. 2001) which do not include any (as yet unknown) dependence of alignments on galaxy luminosity, mass or redshift. Several studies using N-body simulations however find evidence for a dependence of the strength of halo-LSS alignment on mass and redshift (see e.g. Aragón-Calvo et al. 2007; Hahn et al. 2007b; Paz, Stasyszyn & Padilla 2008).

Unfortunately, it is currently still computationally unfeasible to use hydrodynamical simulations of galaxy formation of the necessary resolution in a sufficiently large volume to investigate the correlation function of galaxy shapes and spins. To circumvent this barrier, some authors have used large-volume N-body simulations together with a prescription to assign galactic disc orientations to the DM haloes which typically either assumes perfect alignment with the DM halo spin or some random misalignment angle between the two (e.g. Heymans et al. 2006). Also analytic models based on the halo model have been developed that include prescriptions for small-scale satellite-central alignments (Schneider & Bridle 2010).

Probability distributions for the angles between halo and galaxy spins have been determined by various authors (e.g. van den Bosch et al. 2002; Bailin et al. 2005; Sharma & Steinmetz 2005; Croft et al. 2009; Bett et al. 2010).

Accepting the current unfeasibility of large-volume hydrodynamic simulations, we propose a different approach. Combining local measurements of the alignment of galaxies with the large-scale structure – as has been investigated by Hahn et al. (2007a,b) and Aragón-Calvo et al. (2007) in pure N-body simulations – circumvents the need for large volumes but can still provide constraints on the degree of galaxy alignment to be expected. The results of Navarro, Abadi & Steinmetz (2004) on the basis of four SPH simulations of the formation of single isolated galaxies indicate an alignment of the spin of these galaxies with the intermediate principal axis of the tidal field at turnaround that persists to a slightly weaker degree also to $z = 0$.

In this paper, we study the orientation of a sample of ∼100 galactic discs with respect to their larger scale environment in a hydrodynamical cosmological simulation of the formation of a large filament. We have chosen this particular large-scale environment as it provides an environment where the gravitational shear is expected to be relatively large so that weak lensing shear should have good signal to noise. Any intrinsic alignment of galaxies on these scales will thus impact the measurements through the correlation between intrinsic orientation and gravitational shear (the GI-term). Prior investigations in DM cosmological simulations have shown evidence for alignment of halo spin with filaments. However, considering the gas component rather than DM, the filament is a high-pressure environment so that hydrodynamic effects, such as ram pressure, are expected to play a role in the evolution of the simulated galaxies.

This paper is organized as follows. We describe the details of our numerical simulation, the method to identify galaxies and the selection of galaxies for our analysis in Section 2. We first study the alignments between the gas, stellar, DM angular momenta and the total halo spin in Section 3. Then, we investigate in Section 4 the alignment of the various components with the cosmic large-scale structure, quantitatively described by the tidal field. In Appendix A, we discuss the numerical convergence of our results, before a comparison of our results to observations is given in Section 5. Finally, we summarize and provide our conclusions in Section 6.

2 NUMERICAL METHODS

2.1 Specifics of the cosmological simulation

We simulate the formation of a large cosmic filament and the galaxies embedded in it using the AMR code RAMSES (Teyssier 2002) to evolve DM, gas and stars. Gas dynamics is computed using a second-order unsplit Godunov scheme, particles (DM and stars) are evolved using the particle-mesh method. The simulation includes standard recipes for star formation (Rasera & Teyssier 2006), supernova feedback and chemical enrichment (Dubois & Teyssier 2008). We do not repeat details of these subgrid models but kindly refer the reader to the mentioned papers. The filament was chosen by visual inspection of the environment of the most massive haloes in a dark-matter-only pre-flight simulation. We then chose a filament that is very prominent (and thus relatively massive) and not crisscrossed by too many smaller scale filaments.

Initial conditions were generated using the GRAFIC-2 tool from a power spectrum computed with LINGER. We adopt cosmological parameters as obtained from the *Wilkinson Microwave Anisotropy Probe* (*WMAP*) 5-yr data release (Komatsu et al. 2009), i.e. we use

the density parameters $\Omega_m = 0.276$, $\Omega_b = 0.046$, $\Omega_\Lambda = 0.724$, a power spectrum normalization of $\sigma_8 = 0.811$ and a spectral index $n_s = 0.961$ for the primordial spectrum, as well as a Hubble constant of $H_0 = 100\,h\,\mathrm{km\,s^{-1}\,Mpc^{-1}}$ with $h = 0.703$.

The filament is simulated using the 'zoom-in' technique as a high-resolution region of $25\,h^{-1}\,\mathrm{Mpc}$ diameter at redshift $z = 0$ inside of a comoving $100\,h^{-1}\,\mathrm{Mpc}$ cosmological box. The effective initial resolution of our simulation is 1024^3 particles and grid points inside this high-resolution region, dropping in steps of 8–128^3 in the remainder of the box. Additional refinements are confined to the high-resolution region only. We adopt a refinement strategy based on density threshold so that the number of particles per cell (and the baryon mass per cell) remains roughly constant in time. Since the filament moves slightly in space, we introduce a 'colour' field to mark the Lagrangian volume of the filament. This field is passively advected during the formation of the structures, and thus follows the evolution of the filament perfectly. In order to save memory, we used as colouring variable the metallicity of the gas, with a very low (but non-zero) value of 10^{-3} solar in the high-resolution region and exactly zero outside. Additional refinements are only allowed where the metallicity exceeds one-tenth of this initial value. In addition, cooling and star formation are also switched off in non-coloured regions. The maximum resolution of our simulation is *physical* $0.38\,h^{-1}\,\mathrm{kpc}$ at all times. In addition, our Lagrangian volume excludes the most massive galaxy groups (halo mass above $5 \times 10^{13}\,h^{-1}\mathrm{M}_{sun}$ at $z = 0$) in order to speed up computation as we are only interested in smaller objects in this study.

The two panels of Fig. 1 give a visual impression of the filament at $z = 0$. We show two panels: the first illustrating the distribution of DM; and the second is a composite image representing the density, pressure and metallicity distribution in the gas. Note that the main filament is entirely wrapped by an accretion shock. It is thus clearly a high-pressure environment. The less massive filaments remain cold except at node points where the more massive haloes reside. An inspection of the time-evolution of the simulation reveals that this accretion shock emerges first from the most massive haloes along the filament but then grows along the filament boundaries until the entire filament is enclosed by a shock.

In the two panels of Fig. 2, we show two examples of well-resolved disc-galaxies at $z = 0$ in the simulation. The images represent a simulated stellar light composite image combining the i', r' and g' bands into an Red Green Blue (RGB) image taking into account dust reddening along the line of sight. The images also show the orientation of the stellar and gaseous angular momentum and indicate that these are perpendicular to the discs and well aligned with one another.

2.2 Identification of galaxies

In order to identify galaxies in the simulated data, we directly use the AMR mesh structure and label contiguous volumes exceeding a density threshold. First, we pick the highest refinement level which exceeds $1\,h^{-1}\,\mathrm{kpc}$ resolution in order to smooth out galactic substructure. Next, we keep only those cells on this level, which exceed a threshold $\delta_b = 50\,000$ in baryonic overdensity. This particular choice of δ_b has been found to be in excellent agreement with a visual identification of the galaxies. In a final step, we label all contiguous regions that are left. This labelling is performed using a parallel implementation of the Hoshen–Kopelman cluster finding algorithm (Hoshen & Kopelman 1976). Finally, all star particles and gas cells (also on higher refinement levels) are assigned to the mesh cluster $\mathcal{G}_k$, i.e. the 'galaxy', in which they reside.

Galaxy stellar centres are then determined by iteratively computing the stellar centre of mass within shrinking spherical apertures and moving the aperture to the new centre in each iteration. The procedure is stopped once less than 50 particles are contained within the aperture. The centre of the gaseous disc is defined as the densest gas cell in the galaxy and the centre of the inner DM halo is defined as the most bound DM particle when evaluating the potential for all DM particles that are contained in the galaxy patch.
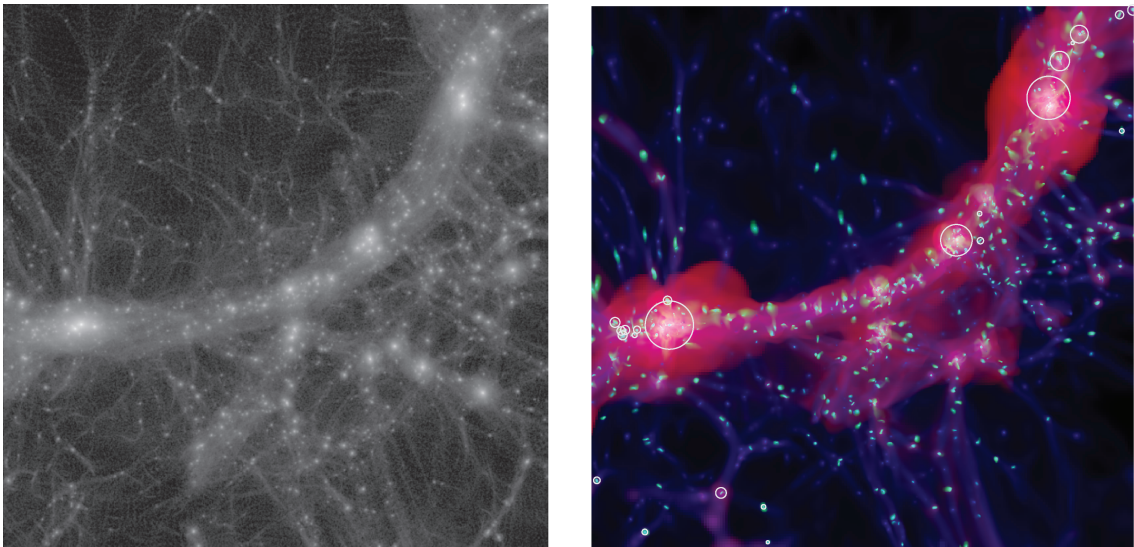

Figure 1. The simulated filament at redshift $z = 0$. The images extend over $20 \times 20\,h^{-2}\,\mathrm{Mpc}^2$ and have a projection depth of $10\,h^{-1}\,\mathrm{Mpc}$. Left-hand panel: the DM particle distribution. Right-hand panel: a composite RGB colour image of the gas distribution, the red image channel was assigned to the pressure, the green channel to the metallicity of the gas and the blue channel to the density. Since metal enriched gas is produced only in galaxies, each of the green blobs corresponds to a galaxy. The white circles in the right-hand panel indicate the virial radii of those host haloes within the filament that have been excluded from refinement for most part of the simulation or are too close to a low-resolution region in the high-resolution run (cf. Section 2.1), and are thus not considered in our analysis. All other galaxies are treated with full resolution and are not affected by low resolution outside of the zoom region.
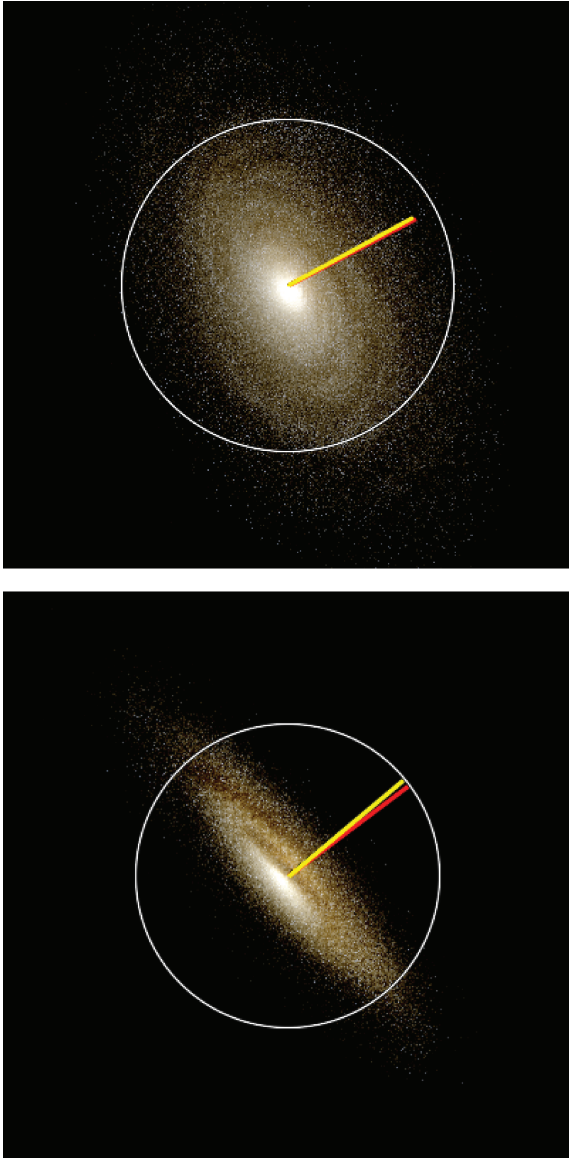
The central galaxies in our samples have stellar radii r_{95} (which is the radius that contains 95 per cent of the stellar mass) that are at most 0.11 at $z = 1$, 0.095 at $z = 0.5$ and 0.077 at $z = 0$ of the virial radius of their parent halo. This makes us confident that the identified galaxies are not contaminated by other satellites in the halo and thus constitute clean samples of central galaxies.

2.3 The fiducial galaxy samples

For our analysis, we keep only the best-resolved galaxies with at least 25000 star particles, corresponding to a minimum stellar mass of $\sim 7.5 \times 10^9 \, h^{-1} \, \mathrm{M}_\odot$. For these galaxies, r_{80}, the radius containing 80 per cent of the stellar mass is resolved by at least eight resolution elements. Furthermore, this requirement implies that we can compare our results to a lower resolution run (see Appendix A) for which the minimum star particle number for galaxies of equal mass is then a factor of 8 lower, but still above 3000.

We split the sample of well-resolved galaxies according to their host halo masses into three different halo groups. The high-mass sample is defined as all haloes above the non-linear mass $M_*(z = 0) \approx 2 \times 10^{12} \, h^{-1} \, \mathrm{M}_\odot$. Prior results using pure N-body simulations have indicated that M_* might be a characteristic scale for the spin-alignment behaviour of DM haloes (see e.g. Aragón-Calvo et al. 2007; Hahn et al. 2007b; Paz et al. 2008). The intermediate sample is for halo masses smaller than this non–linear mass, but larger than the 'cold accretion limit' of $\sim 4 \times 10^{11} \, h^{-1} \, \mathrm{M}_\odot$ (see e.g. Birnboim & Dekel 2003; Kereš et al. 2005; Dekel & Birnboim 2006). Haloes above this critical mass are believed to host a hot pressurized atmosphere that can exert ram-pressure effects on the central galaxy. The third mass sample is for halo masses smaller than the critical mass. Note that for the two higher redshifts $z = 1$ and 0.5, we merge together the high and intermediate mass samples to improve statistical significance. Detailed information about the galaxy samples is given in Table 1. The distribution of stellar masses in the samples is shown in Fig. 3.

2.4 Measured galactic properties

In this study, we are interested in the orientation of disc galaxies. Since we exclude the most massive (large group-scale and above) haloes from refinement, indeed all galaxies considered are discy. We can thus simply quantify the disc orientation by the angular momenta of the various disc constituents: gas, stars and DM.

We compute the angular momentum for each galaxy $\mathcal{G}_k$ by evaluating the sum,

$$\boldsymbol{J}_k = \sum_{i \in \mathcal{G}_k} m_i (\boldsymbol{r}_i - \bar{\boldsymbol{r}}_k) \times (\boldsymbol{v}_i - \bar{\boldsymbol{v}}_k), \tag{1}$$

where $\bar{\boldsymbol{r}}_k$ is the stellar centre of the kth galaxy inner region (see previous section), and $\bar{\boldsymbol{v}}_k$ is the centre of mass velocity. The sum is evaluated separately for all star particles that are part of an identified galaxy $\mathcal{G}_k$ to yield the stellar angular momentum $\boldsymbol{J}_k^{\mathrm{S}}$, as well as for all DM particles that are contained within a sphere of the radius of the most distant star particle in the galaxy $\boldsymbol{J}_k^{\mathrm{DM}}$. Finally, we also compute the gas angular momentum $\boldsymbol{J}_k^{\mathrm{G}}$ by summing over all leaf cells of the AMR tree that are contained in the galaxy (and are thus effectively bounded by an isodensity surface – see Section 2.2 for details). For gas, $\bar{\boldsymbol{r}}_k$ refers to the densest cell in the galaxy patch and $\bar{\boldsymbol{v}}_k$ to the centre of mass velocity computed over all leaf cells in $\mathcal{G}_k$, while for DM $\bar{\boldsymbol{r}}_k$ refers to the most bound DM particle and $\bar{\boldsymbol{v}}_k$ to the centre of mass velocity of the DM particles in the sphere containing $\mathcal{G}_k$ (see also Section 2.2). In order to determine the total

Figure 2. Simulated stellar light composite images of two well-resolved disc-galaxies using the i', r' and g' band light and taking into account dust absorption. The white circles correspond to the radius containing 95 per cent of the stellar mass. The yellow line corresponds to the stellar angular momentum vector direction, the red line to the gas angular momentum.

In order to determine halo masses and virial radii, we grow spheres around each galaxy centre until the enclosed matter overdensity falls below the overdensity Δ_c of a virialized spherical perturbation in a Λ cold dark matter cosmology as given by the fitting formula of Bryan & Norman (1998). In a next step, we determine equivalence classes of galaxies that are contained within the virial radii of each other. The galaxy with the highest stellar mass in each equivalence class we call the 'central galaxy', all other class members are 'satellite galaxies'. We do not consider these satellite galaxies further in this study.

Finally, unresolved galaxies are identified by tracking the DM particles that end up in galaxies back to the initial conditions and requiring that none of them started in a region that was not initially marked for cooling and refinement. These unresolved galaxies are then removed from the galaxy catalogue.

Table 1. The galaxy samples used in our analysis. We split central galaxies according to their host halo mass in a low mass (LM) and high mass (HM) bin at redshifts $z = 1$ and 0.5 and an additional medium mass (MM) bin at $z = 0$. For each mass bin and each redshift, the median stellar mass as well as the number of galaxies in the bin is given. See Fig. 3 for histograms of stellar masses for each of the galaxy samples.

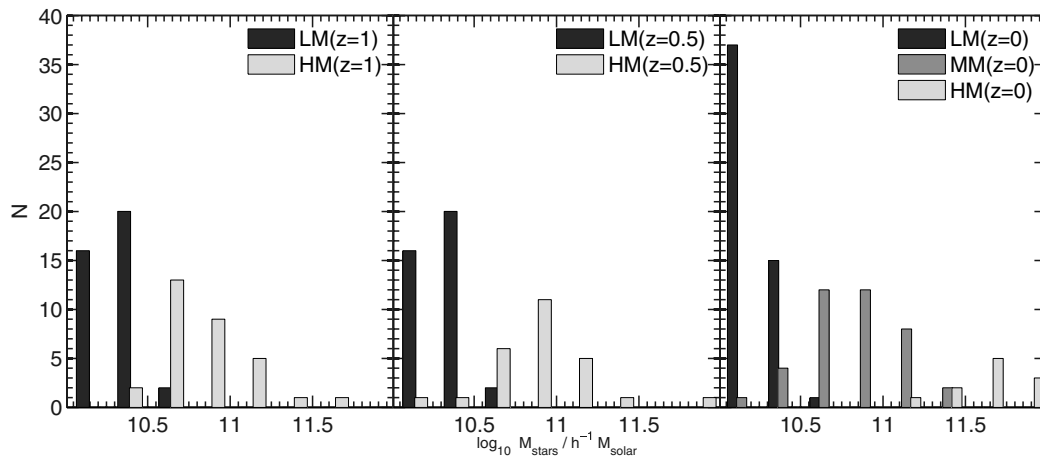|	LM	MM	HM
$z = 0$:			
$M_{halo} / h^{-1} M_{\odot}$	1–4×10^{11}	5×10^{11}–2×10^{12}	$> 2 \times 10^{12}$
Median $M_{stellar} / h^{-1} M_{\odot}$	1.3×10^{10}	6.8×10^{10}	4.2×10^{11}
Number of galaxies	70	39	12
$z = 0.5$:			
$M_{halo} / h^{-1} M_{\odot}$	1–4×10^{11}	-	$> 4 \times 10^{11}$
Median $M_{stellar} / h^{-1} M_{\odot}$	1.3×10^{10}	-	6.7×10^{10}
Number of galaxies	48	-	28
$z = 1$:			
$M_{halo} / h^{-1} M_{\odot}$	1–4×10^{11}	-	$> 4 \times 10^{11}$
Median $M_{stellar} / h^{-1} M_{\odot}$	1.3×10^{10}	-	6.3×10^{10}
Number of galaxies	58	-	31

Figure 3. Distributions of galaxy stellar masses in the two/three galaxy samples used in our analysis (see Table 1 for details) at redshifts $z = 1$ (left-hand panel), $z = 0.5$ (middle panel) and $z = 0$ (right-hand panel).

halo angular momentum, we evaluate equation (1) summing over all components and up to the virial radius to obtain J_{tot}.

2.5 Quantifying large-scale structure with the tidal field

In analogy to the approach followed by Hahn et al. (2007a,b), we use the eigenvectors of the tidal field tensor smoothed on some scale R_s to probe alignments with the large-scale structure. This approach has two main advantages: (1) as demonstrated in Hahn et al. (2007a), the tidal field provides a natural dynamical quantification of the geometry of the large-scale structure; and (2) any local alignments with the tidal field directly translate into shear–ellipticity alignments in weak lensing (Hirata & Seljak 2004). In addition, when supplemented with autocorrelation functions of the non-linear tidal field (see Lee, Hahn & Porciani 2009b), local alignments with the tidal field can be translated into correlation functions. We will investigate this approach in future work.

We determine the tidal field by first constructing the full matter overdensity field $\delta(\boldsymbol{x})$ of the entire simulation volume on a 512^3 grid. This grid is subsequently smoothed with a Gaussian kernel of varying filtering radius R_s. Finally, we solve Poisson's equation using the fast Fourier transform to obtain the potential $\phi(\boldsymbol{x})$, evaluate

the Hessian matrix $T_{ij} \equiv \partial_i \partial_j \phi$ by finite differencing the potential and interpolating via cloud-in-cell to the galaxy positions. Diagonalizing T_{ij} at each galaxy's position, we find the three eigenvalues $\lambda_3(R_s) \leq \lambda_2(R_s) \leq \lambda_1(R_s)$ and the corresponding unit eigenvectors $\boldsymbol{v}_3(R_s)$, $\boldsymbol{v}_2(R_s)$, $\boldsymbol{v}_1(R_s)$ as a function of the applied filtering scale R_s. Note that we define T_{ij} to be simply the Hessian of the potential, i.e. the signs of the eigenvalues might be reversed with respect to some other studies.

The eigenstructure of the Hessian of the gravitational potential is intimately connected to the large-scale dynamics of the cosmic web. Filamentary regions tend to have one negative and two positive eigenvalues when smoothed on large-enough scales. In particular, we find e.g. average values $\langle \lambda_3 \rangle = -0.2$, $\langle \lambda_2 \rangle = 0.2$ and $\langle \lambda_1 \rangle = 0.6$ on scales of comoving $3\,h^{-1}$ Mpc where the averages are taken over the sample of our galaxies at $z = 0.5$. Units are such that $\sum_i \lambda_i = \delta$, where δ is the matter overdensity. The signature of these eigenvalues indicates that the galaxies are, on average, indeed embedded in a filamentary environment. The signs of the eigenvalues reflect the large-scale expansion along the filament – corresponding to the direction indicated by the eigenvector of the negative eigenvalue λ_3 – and gravitational contraction in the perpendicular plane – corresponding to the plane spanned by the eigenvectors $\boldsymbol{v}_2$ and $\boldsymbol{v}_1$. The
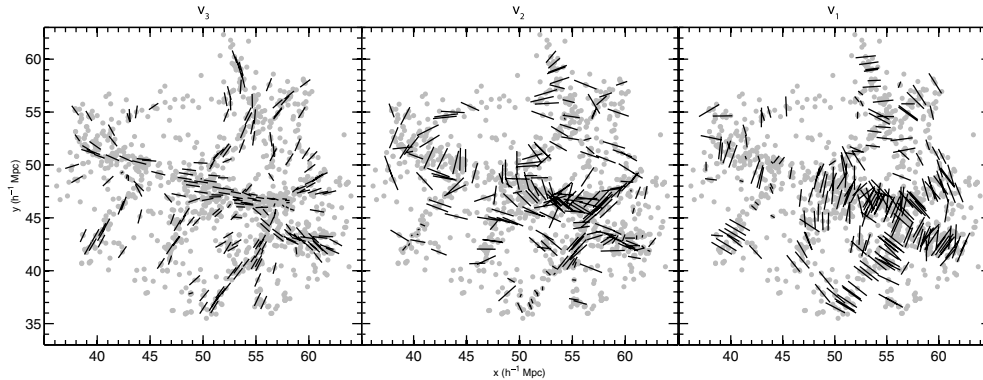
Figure 4. Directions of the tidal field eigenvectors at $z = 0.5$ for a smoothing scale of $R_s = 2\,h^{-1}$ Mpc physical ($3\,h^{-1}$ Mpc comoving). The $\mathbf{v}_3$ eigenvector indicates the overall direction of the filaments, while $\mathbf{v}_2$ and $\mathbf{v}_1$ span the perpendicular plane. Linear tidal torque theory favours alignment of galactic spin with $\mathbf{v}_2$.
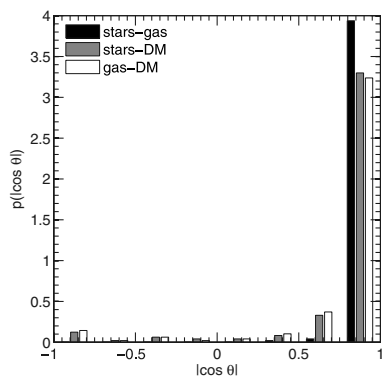

Figure 5. Distribution of angles between the angular momentum vectors of the stellar, gas and DM component within the blob that identifies the galaxy. The angle distributions are shown for the entire sample of well-resolved central galaxies.

Table 2. Upper half: median alignment angles between the gas (G), stellar (S) and DM component of the galactic disc at redhifts $z = 0, 0.5$ and 1. Lower half: median alignment angles between the three components of the galactic disc and the total angular momentum of the host halo. Errors are non-symmetric uncertainties on the median (see text for more details). Values are given for the entire sample of well-resolved central galaxies since no mass dependence was found.

Median	$z = 0$	$z = 0.5$	$z = 1$
$\cos\theta_{S,G}$	$0.993^{+0.001}_{-0.003}$	$0.992^{+0.001}_{-0.003}$	$0.991^{+0.001}_{-0.003}$
$\cos\theta_{S,DM}$	$0.967^{+0.002}_{-0.013}$	$0.932^{+0.006}_{-0.018}$	$0.827^{+0.013}_{-0.072}$
$\cos\theta_{G,DM}$	$0.949^{+0.004}_{-0.017}$	$0.914^{+0.008}_{-0.025}$	$0.817^{+0.016}_{-0.070}$
$\cos\theta_{S,tot}$	$0.657^{+0.022}_{-0.062}$	$0.690^{+0.027}_{-0.064}$	$0.674^{+0.023}_{-0.068}$
$\cos\theta_{G,tot}$	$0.652^{+0.023}_{-0.068}$	$0.667^{+0.029}_{-0.058}$	$0.711^{+0.020}_{-0.063}$
$\cos\theta_{DM,tot}$	$0.712^{+0.023}_{-0.055}$	$0.761^{+0.021}_{-0.072}$	$0.827^{+0.013}_{-0.087}$

connection between the eigenstructure of T_{ij} and dynamics follows readily from the Zel'dovich theory of pancake collapse (Zel'dovich 1970). In Fig. 4, we show the orientations of the eigenvectors with respect to the cosmic web structure.

To summarize, $\mathbf{v}_3$ indicates the overall direction of a filament, while $\mathbf{v}_2$ and $\mathbf{v}_1$ span the perpendicular plane. A more detailed account is given in Hahn et al. (2007a).

3 THE DISTRIBUTION OF ANGULAR MOMENTUM IN GALAXIES

3.1 Angular momentum correlations within the galaxy

In Fig. 5 , we show the distributions of angles θ between the angular momentum vectors of the stellar (S), gas (G) and DM component within well-resolved central galaxies at $z = 0$ (the nomenclature is such that, e.g. $\theta_{S,G}$ is the angle between the stellar and gas angular momentum vectors). The corresponding median angles are given for $z = 0$–1 in Table 2 (upper half) together with the error on the median. We compute the upper error σ_u and lower error σ_l as

$$\sigma_u = \frac{\theta_{84} - \theta_{50}}{\sqrt{N}}, \quad \sigma_l = \frac{\theta_{16} - \theta_{50}}{\sqrt{N}}, \quad (2)$$

where subscripted numbers indicate percentiles and N is the number of galaxies considered.

Within the galactic discs (which is defined by the mesh cluster identified as a single galaxy – see Section 2.2 – and thus has no imposed symmetry for the stars and the gas), the gas angular momentum deviates by a median of $8°$ from that of the stars. The difference with respect to the DM angular momentum, which was determined in a sphere around the disc, is slightly higher at around $18°$ at $z = 0$ for both stars and gas and increases to around $36°$ at $z = 1$.

We find no correlation between these alignment angles and either stellar or host halo mass with a significance above 1σ. This is a comforting result as stellar mass is directly proportional to the number of star particles and the lack of a correlation demonstrates the absence of an obvious resolution problem. We discuss numerical convergence of our results in more detail in Appendix A.

3.2 Angular momentum correlations between central galaxies and their host halo

In Fig. 6, we show the distribution of angles between the angular momentum vector of the host DM halo (determined out to the virial radius from both baryonic and DM) and the inner components (determined at the disc) for the three redshifts at which we perform our analysis. Galaxies from all samples have been combined. The corresponding median angles and the width of the distributions are given in Table 2.
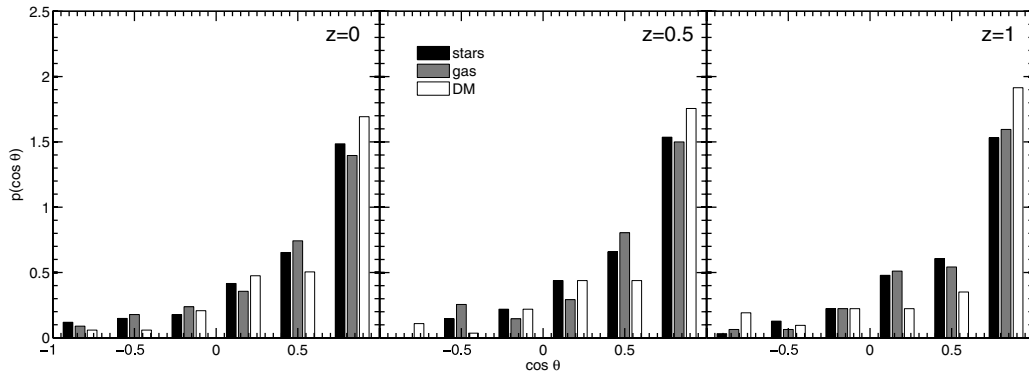
Figure 6. Distribution of angles between the total (DM plus baryonic) angular momentum vectors of the DM host halo and the stellar, gas and DM component of the central galaxy. The angle distributions are shown for the entire sample of well-resolved central galaxies at $z = 0$ (left-hand panel), $z = 0.5$ (centre panel) and $z = 1$ (right-hand panel).

We find a fairly broad distribution of angles with the host angular momentum deviating by $\sim 50°$ at $z = 0$ from either the stellar or gas spin of the central galaxy. Our results indicate that this discrepancy decreases slightly to about $46°$ at $z = 1$. The value we find for the stellar component is in excellent agreement with the results found by Croft et al. (2009) who report a median angle for the stellar component of $44°$ and $70°$ for the gas. The quoted larger angle for the gaseous component is possibly due to satellites that are included in the sample of Croft et al. (2009) and for which ram pressure modifies the gas disc orientations very quickly. It appears, however, that our results are in slight tension with the recent findings of Bett et al. (2010) who report a smaller median angle of $34°$ between galaxy and outer DM halo at $z = 0$. It remains a matter of future studies to better quantify the influence of resolution and feedback recipes on these results. A further possible origin for the discrepancy between our results and those of Bett et al. (2010) might lie in the difference of large-scale environment. While we simulate the relatively high-pressure environment of a massive filament, the galaxy sample considered by Bett et al. (2010) has a halo mass upper limit of $1.6 \times 10^{12} \, M_\odot$, suggesting that they reside in a lower density environment with a more quiescent formation history.

The outer and inner DM spins are significantly stronger aligned than the baryonic components. We find a median angle of $\sim 45°$ at $z = 0$ which decreases to $\sim 34°$ at $z = 1$. Again, we find no correlation between the alignment angles and either stellar or host halo mass with a significance above 1σ.

4 THE LARGE-SCALE ORIENTATIONS OF GALAXIES

4.1 Predictions of analytic models

The linear tidal torque theory predicts that the angular momentum of a protogalaxy is determined by its geometric shape and the tidal field exerted by the larger scale environment (e.g. Peebles 1969; White 1984; Porciani, Dekel & Hoffman 2002). In particular, angular momentum is generated from the misalignment of the Lagrangian moment of inertia tensor I_{ij} and the Lagrangian tidal tensor T_{ij}, so that at first order

$$J_i \propto \epsilon_{ijk} T_{jl} I_{lk}, \tag{3}$$

where ϵ_{ijk} is the Levi–Civita symbol. In the eigenspace of the tidal tensor, the components of $\boldsymbol{J}$ become

$$J_1 \propto (\lambda_2 - \lambda_3) I_{23},$$
$$J_2 \propto (\lambda_3 - \lambda_1) I_{31},$$
$$J_3 \propto (\lambda_1 - \lambda_2) I_{12}. \tag{4}$$

Since, by definition, $\lambda_3 - \lambda_1$ is the largest coefficient, linear tidal torque theory thus predicts that, at first order, $\boldsymbol{J}$ is preferentially aligned with $\boldsymbol{v}_2$ in a statistical sample of haloes/galaxies where contributions from the moment of inertia tensor average out and T_{ij} and I_{ij} are assumed to be uncorrelated. Moreover, generation of angular momentum is most efficient at turnaround when the I_{ij} is maximal.

However, the assumption that T_{ij} and I_{ij} are uncorrelated is not well justified, as the two tensors are indeed found to be correlated (see e.g. Porciani, Dekel & Hoffman 2002; Lee, Hahn & Porciani 2009a). Thus, it is particularly interesting to see whether the alignment predicted from Lagrangian perturbation theory is indeed present in hydrodynamic cosmological simulations, and particularly so at late times well after turnaround of the protogalaxy.

Lee & Erdogdu (2007) have derived a probability distribution for the angle $\cos \theta_2 = |\boldsymbol{J} \cdot \boldsymbol{v}_2| / \|\boldsymbol{J}\|$ – along which the possibly strongest alignment could be observed – of the form

$$p(\cos \theta_2) = (1 + c) \sqrt{1 - \frac{c}{2}} \left[1 + c \left(1 - \frac{3}{2} \cos^2 \theta_2 \right) \right]^{-3/2}, \tag{5}$$

where c is a normalization parameter.

4.2 The distribution of spin and tidal field eigenvectors

4.2.1 Anisotropy of the tidal field

In Fig. 7, we show the spatial distribution at $z = 0.5$ of tidal field eigenvectors $\boldsymbol{v}_{1-3}$ for the comoving smoothing scales $R_s = 1, 2$ and $5 \, h^{-1}$ Mpc in Mollweide projection. The tidal field is evaluated at the positions of the galaxies that are included in any of the samples (LM or HM). As this is an equal-area projection, local concentrations directly translate into an increased anisotropy for that direction. Since the tidal field is a tensor field, each vector has spin-two symmetry and hence is represented by two points, the second being a reflection of the first at the origin. While the tidal field is already highly anisotropic on scales of $1 \, h^{-1}$ Mpc, on scales of $5 \, h^{-1}$ Mpc virtually only the main filament remains so that the distribution of eigenvectors becomes almost dipolar.
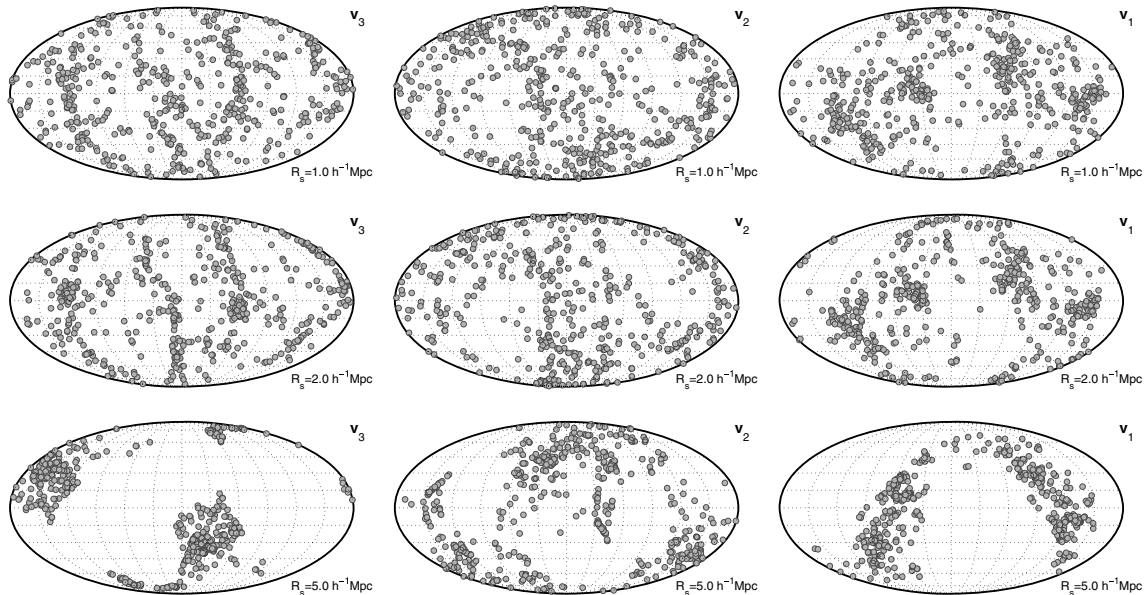
Figure 7. Mollweide sphere projections of the three eigenvalues of the tidal field at the positions of the galaxies for three smoothing scales, $1\,h^{-1}$ Mpc (top panels), $2\,h^{-1}$ Mpc (middle panels) and $5\,h^{-1}$ Mpc (bottom panels). All data are for redshift $z = 0.5$. Since the tidal field has a spin-two symmetry, each vector is represented by two points. The Mollweide projection is an area preserving projection.

4.2.2 Anisotropy of the galaxy spin distribution

Fig. 8 shows the distribution of stellar angular momentum vectors at redshifts $z = 1$, 0.5 and 0 in Mollweide projection. At all redshifts, the distributions are clearly anisotropic. The origin and detailed form of this anisotropic distribution is determined by both physical and numerical effects. We will discuss their interaction in what follows.

At $z = 1$, the distribution is anisotropic with no clear clustering of spin vectors around the Cartesian grid vectors. This provides strong evidence that the high-redshift spin distribution is anisotropic due to physical processes. Comparing with Fig. 6, the tidal field on scales $<5\,h^{-1}$ Mpc is anisotropic at a similar level. We will discuss their cross-correlation in the next section.

At $z = 0.5$, there is a slight tendency for the spins to cluster around the grid vectors that is more obvious at $z = 0$ for the low-mass galaxies. Since a multigrid Poisson solver (such as the one used in RAMSES) introduces preferred directions along the Cartesian grid basis vectors, a non-physical anisotropy of the gravitational interparticle force is expected close to the resolution limit (cf. Hockney & Eastwood 1981) arising from an unavoidable lack of symmetry in the discrete Laplacian operator. These errors are systematic in any asymmetric system (cf. May & James 1984). This is clearly a systematic effect in our numerical results, and we need to estimate its magnitude.

Remarkably, the grid-aligned galaxies at low redshift are not distributed isotropically among all Cartesian grid vectors. In larger scale simulations of entire cosmological volumes (i.e. not restricted to a filamentary region – as e.g. in the 'Mare Nostrum' simulation; Ocvirk et al. 2008), we do not see this effect. In these larger volume simulations at lower spatial resolution, grid-alignment is also observed but with galaxies aligned with all three grid vectors.

Given the highly anisotropic distribution of tidal field eigenvectors (see previous subsection), it is however clear how such an anisotropy can arise. Assuming that the galaxies' orientations are determined by some anisotropic physical effect (such as tides), the discs' initial angular momentum will be anisotropic (as it is at $z = 1$). Given the additional numerical anisotropy, the discs will subsequently relax slowly to the closest potential minimum, i.e. the closest Cartesian grid vector, in the absence of any perturbation that is larger than the numerical error (and thus predominantly in low density regions). This will happen on a time-scale that is connected to the anisotropy of the error in the multigrid Poisson solver. Support for this interpretation of the numerical results comes from a look at the galaxies' spin distribution at high redshift where no obvious grid-alignment is observed. Looking at the left-hand panel of Fig. 8, we see a non-isotropic distribution with no spins in the vicinity of those grid axes where by $z = 0$ also no grid-aligned galaxies are seen (e.g. the one in the very centre of the Mollweide maps).
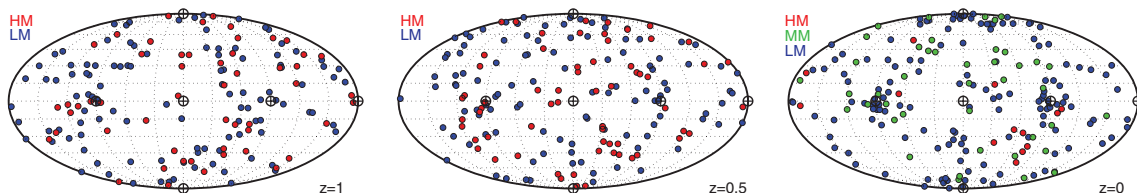

Figure 8. The orientations of galaxy stellar angular momenta at redshifts $z = 1$ (left panel;), $z = 0.5$ (middle panel) and $z = 0$ (right panel). The angular momentum vectors are shown in the Mollweide projection. The circled crosses indicate the Cartesian basis vectors of the AMR grid.

We will continue to discuss the impact of such a spurious alignment on our results in Appendix A. To conclude this section, we can however clearly say that the distribution of galaxy angular momenta is anisotropic due to galaxy formation physics. The anisotropy is then likely amplified by numerical effects at low redshifts, but numerical effects alone will never generate an anisotropic distribution.

4.3 Correlations with the tidal field

As outlined in Section 4.1, linear tidal torque theory indicates that galaxies might show a preferential alignment with the intermediate principal axis of the tidal field. In this section, we investigate whether such an alignment persists also at times after the turnaround of the protogalaxy in our simulation. Unfortunately, the scale on which the tidal field should be computed is not known a priori so that we present the degree of alignment for a range of smoothing scales. Since these scales are likely to be different for galaxies of different masses, and galaxies of different halo masses may also experiences differences in the details of their formation, all results are split into different halo masses as described in Section 2.3. In addition, we distinguish low-mass galaxies in high-density and in low-density environments.

In Fig. 9, we show the scale dependence of the cosine of the angles $|\cos\theta_i|$ between the angular momentum vectors of the galaxies and the tidal field eigenvectors $\boldsymbol{v}_i$ for the inner DM, gas and stellar components. The panels represent the alignments with the three eigenvectors (vertical) for the two mass bins (horizontal). We additionally split the low mass bin (LM) into an overdense bin $\delta > \delta_{50}$ and an underdense bin $\delta < \delta_{50}$, where here δ is the matter overdensity field smoothed on a $2\text{-}h^{-1}$ Mpc physical scale, and δ_{50} is the median overdensity for the galaxies in the respective mass bin. The values of δ_{50} for our sample of galaxies turn out to be: 0.27 at $z = 1$, 0.54 at $z = 0.5$ and 1.16 at $z = 0$.

Using a two-tailed Kolmogorov–Smirnov test, we assess the inconsistency of the angle distributions on a scale of physical $2\,h^{-1}$ Mpc with a flat (i.e. random distribution) $p_{\text{rand}}(|\cos\theta_i|) = 1$. The significance levels are given in units of σ in Table 3.

At $z = 1$, we find the strongest alignment for the low-mass low-density sample, where on scales of physical $2\,h^{-1}$ Mpc, the alignment signal with the intermediate principal axes of the tidal field peaks at a median angle of $|\cos\theta_2| \sim 0.7$ for the stellar angular momentum component. The deviation from a random angle distribution is significant at 2.75σ. The alignment of the gas disc is slightly weaker, while that of the inner DM is slightly stronger. There is a weaker counteralignment with the third principal axis on these scales, while the alignment with the first axis is consistent with random.

For the low-mass high-density sample, we find a significant alignment only with the first principal axis for the stellar and gas
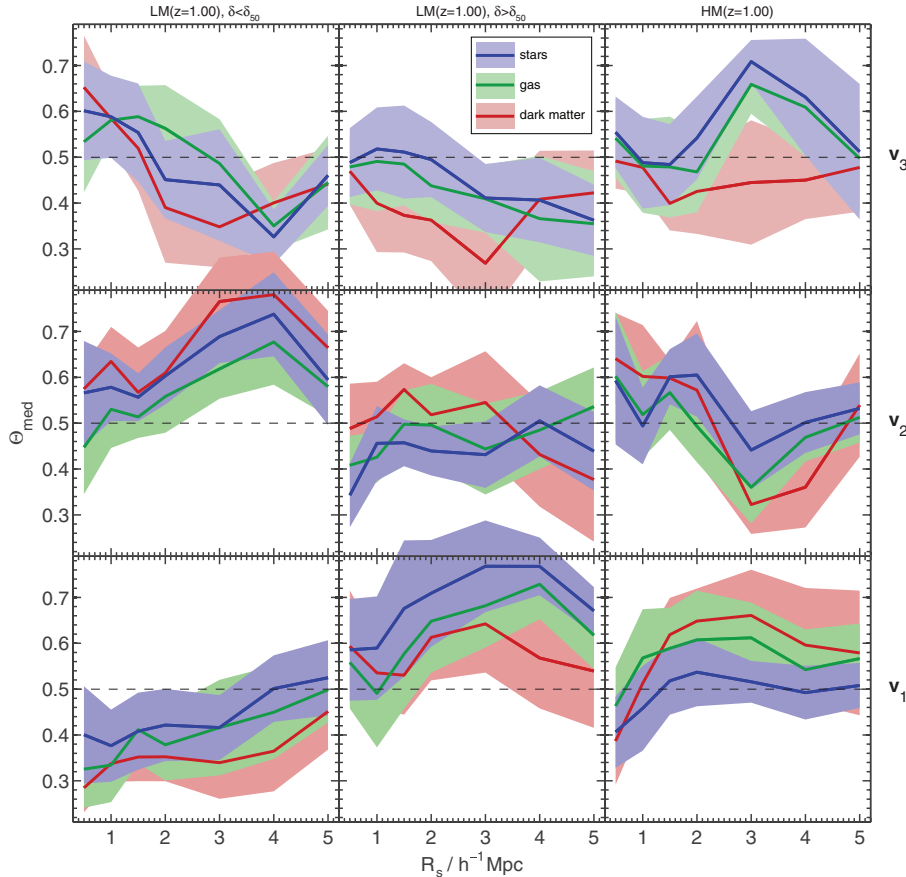

Figure 9. Median cosine at $z = 1$ of the angle between the spin of the DM (red), gaseous (green) and stellar (blue) component of central galaxies and the three eigenvectors of the tidal field tensor as a function of the scale R_s (given in h^{-1} Mpc comoving) on which the tidal field was smoothed. The data are shown in for the halo mass bins given in Table 1 with the low mass (LM) sample split into two samples above and below the median environmental matter overdensity determined on physical scales of $2\,h^{-1}$ Mpc (i.e. $4\,h^{-1}$ Mpc comoving). The shaded areas represent the 1σ uncertainty on the median obtained with 200 bootstrap resamplings.

Table 3. Significance levels for the rejection of the null-hypothesis that the angle distributions between the spin of the gas disc (G), stellar disc (S) or inner DM with the tidal field eigenvectors are consistent with a uniform distribution $p(|\cos\theta_i|) = 1$ obtained with the Kolmogorov–Smirnov test. The tidal field was smoothed on a scale of physical $2\,h^{-1}$ Mpc for this test. Boldface numbers highlight those correlations that have a significance above 2σ.

Significance in units of σ	$z = 1$ LM $\delta < \delta_{50}$	LM $\delta > \delta_{50}$	HM	$z = 0.5$ LM $\delta < \delta_{50}$	LM $\delta > \delta_{50}$	HM	$z = 0$ LM $\delta < \delta_{50}$	LM $\delta > \delta_{50}$	MM	HM
$\theta_{3,G}$	0.60	1.96	0.22	**2.26**	0.02	0.18	0.29	0.24	0.46	0.80
$\theta_{2,G}$	**2.30**	1.07	0.26	**2.27**	0.15	0.52	0.01	0.92	1.06	0.45
$\theta_{1,G}$	1.93	1.20	0.55	0.94	0.34	1.06	0.49	0.11	0.32	1.53
$\theta_{3,S}$	1.14	**2.97**	0.55	**2.58**	0.23	0.13	0.40	0.05	0.02	0.59
$\theta_{2,S}$	**2.75**	1.28	0.20	1.66	0.30	0.29	0.73	0.29	1.21	0.41
$\theta_{1,S}$	**2.21**	0.67	1.06	0.38	0.22	0.51	1.00	0.26	1.01	1.61
$\theta_{3,DM}$	1.28	0.32	0.69	1.98	1.46	0.68	0.01	0.72	0.36	0.92
$\theta_{2,DM}$	**3.43**	1.05	1.21	1.56	0.11	0.94	1.72	0.40	0.38	0.79
$\theta_{1,DM}$	1.28	1.45	0.58	0.19	0.39	0.25	1.75	0.24	0.94	1.05

component, while the DM angular momentum is consistent with random at almost all scales.

Finally, for the high-mass sample, we find a significant alignment of the stellar and gas component with the third principal axis on comoving scales of $3\,h^{-1}$ Mpc which is however not seen for the inner DM component at $z = 1$. At lower redshifts, this alignment decreases slightly, but is also seen for the DM component.

In Fig. 10, we show the scale-dependent median alignment for the $z = 0.5$ samples of galaxies. As for the $z = 1$ sample, we again find a preferential alignment of the low-mass low-density sample

with the intermediate axis of the tidal field peaking on scales of physical $2\,h^{-1}$ Mpc and a counteralignment with the first principal axis. For the low-mass high-density environment, our findings are consistent with random. There is again a weak tendency for the high-mass sample to be aligned with the third principal axis.

In Fig. 11, we show the scale dependent median alignment for the $z = 0$ samples of galaxies. For the low-mass samples, all alignment signals are consistent with random. For the medium mass sample, we find a very weak tendency for alignment with the intermediate principal axis of the tidal field. The high-mass sample shows a
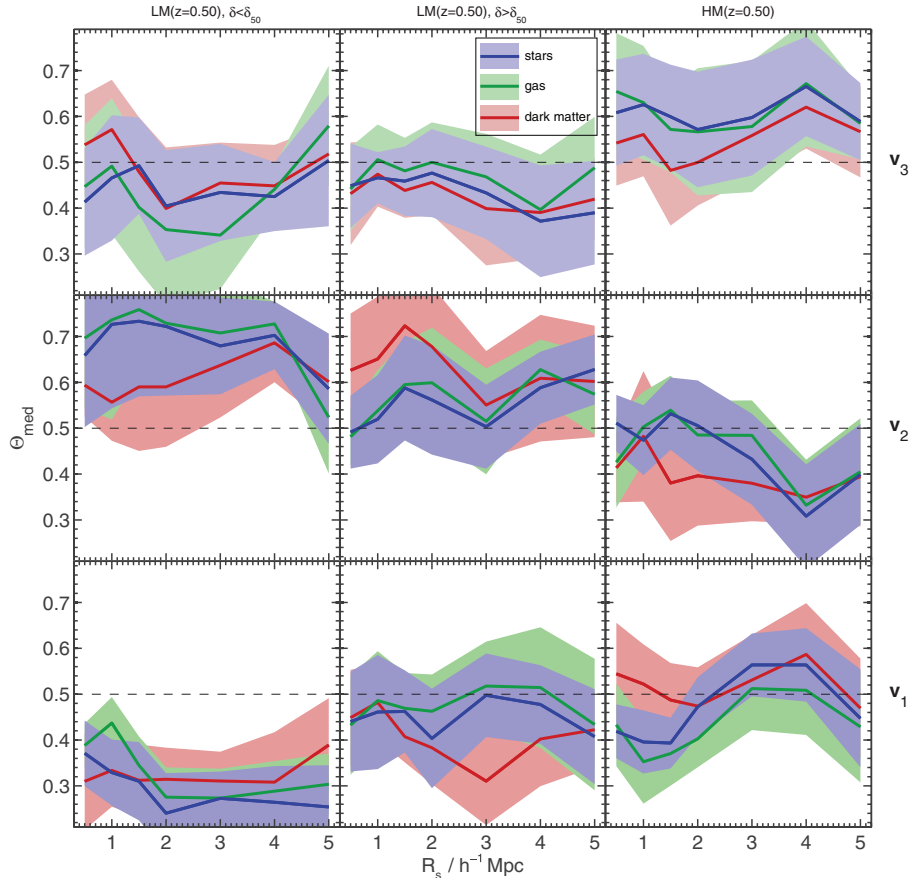

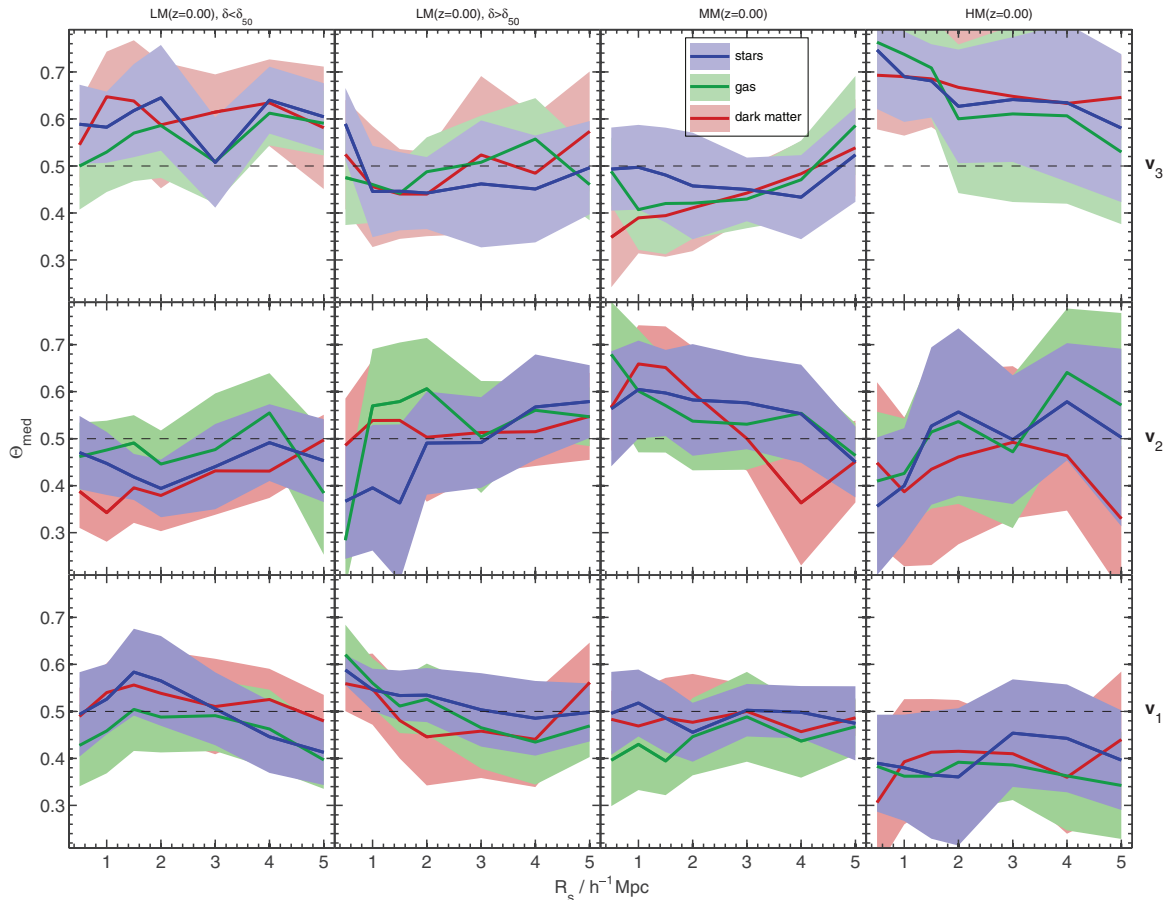**Figure 10.** Same as Fig. 9 but at redshift $z = 0.5$.

Figure 11. Same as Fig. 9, but at redshift $z = 0$.

significant alignment with the third principal axis on small scales $\lesssim 1\,h^{-1}$ Mpc that is still present but weakens at larger scales. Note, however, that the high-mass sample consists only of 12 galaxies.

4.4 Alignment angle probability distributions

Figs 12–14 show the probability distributions $p(|\cos\theta_i|)$ for the low-mass samples (LM) at redshifts $z = 1$, 0.5 and 0, respectively. The galaxy samples have again been split into a high and low environment density sample above and below the median density, as described in Section 4.3, and the angle distributions are given for the same scale on which the density field has been obtained – $2\,h^{-1}$ Mpc physical at all redshifts.

For the higher redshifts $z = 1$ and 0.5, the low-density sample is consistent with the model fit for spin alignment with the intermediate axis of the tidal field given by Lee & Erdogdu (2007) albeit for a parameter which is significantly larger (roughly a factor of 9) than the best-fitting value to the Two Micron All Sky Survey (2MASS) galaxy samples obtained in their study. While this discrepancy might seem large, it is not clear to what extent our samples are comparable at all with the observational data from the 2MASS survey. Furthermore, the weaker alignment seen in observational data might be due to the inherent difficulty to infer the orientation of a galaxy from the projected image, as well as uncertainties in determining the tidal field.

More curiously, however, Lee & Erdogdu (2007) find a stronger alignment signal with the intermediate axis for galaxies in high-density regions. At all redshifts, for the high-density sample of low-mass galaxies, our results are consistent with random orientations. While tidal torque theory predicts that alignment with the intermediate axis should indeed be stronger in high-density regions (Lee & Erdogdu 2007), our results do not support that this prediction is valid in highly non-linear environments.

4.5 The impact of environment on alignments

In Fig. 15, we show the dependence on environmental density of the alignment angles of the galaxies' stellar angular momentum with the three principal axes of the tidal field for the low-mass sample of galaxies at redshift $z = 1$. The overdensity field δ is evaluated on the scale of $R_s = 2\,h^{-1}$ Mpc physical.

We find that the alignment of stellar angular momentum with the intermediate axis decreases strongly when the environmental density increases. This is perfectly consistent with our the results from Fig. 9 that no alignment with the intermediate axis is present for haloes in regions above the median environmental overdensity. On the other hand, the alignments with the first and the third axis increase with the overdensity of the environment.

All three relations between δ and the three $|\cos\theta_i|$ are significant. In particular, we find Spearman rank correlation coefficients of 0.32 with 2.47σ significance for θ_3, -0.38 with 2.96σ significance for θ_2 and 0.24 with 1.81σ significance for θ_1. We find quantitatively identical but weaker and slightly less significant correlations also at $z = 0.5$.
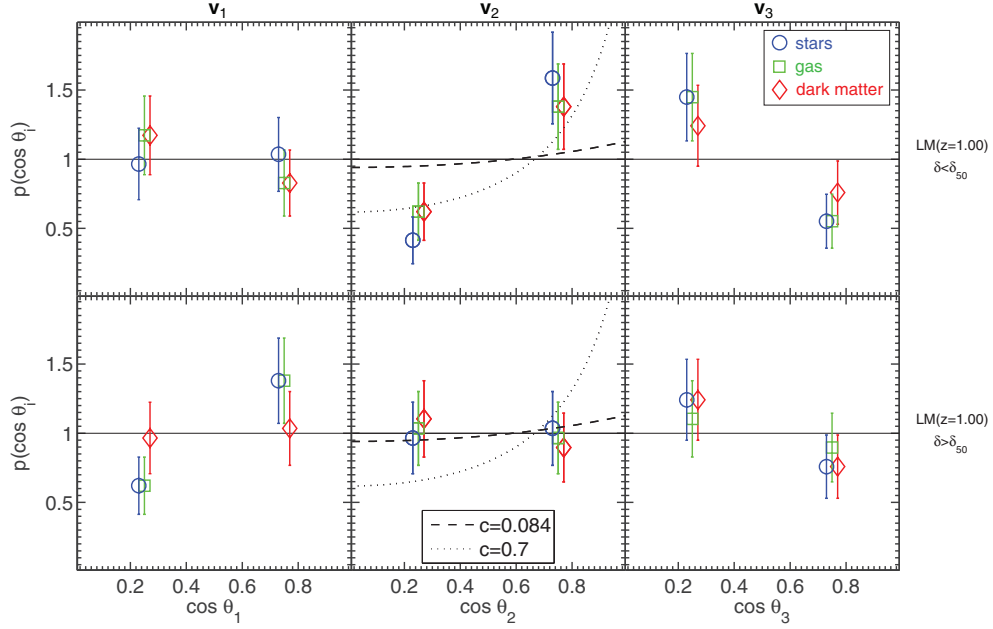
Figure 12. The distribution of $|\cos\theta_i|$ between the galaxy spin vector and the three eigenvectors v_3 (left-hand panel), v_2 (middle panel) and v_1 (right-hand panel) at $z = 1$. Shown is the binned median, error bars correspond to the Poisson error on the median. The distributions are shown for the stellar (blue circles), gaseous (green squares) and DM (red diamonds) components of the galaxies. The dashed and dotted line indicate the model predictions from Lee & Erdogdu (2007).The dashed line corresponds to the observationally determined fit of the model as given in Lee & Erdogdu (2007), while the dotted line corresponds to the model with $c = 0.7$. In each plot, the top panel shows the distribution for the low-mass low-density (LM, $\delta < \delta_{50}$) sample, and the lower the distribution for the low-mass high-density (LM, $\delta > \delta_{50}$) sample. Density and alignments have been determined on scales of $2\,h^{-1}$ Mpc physical.
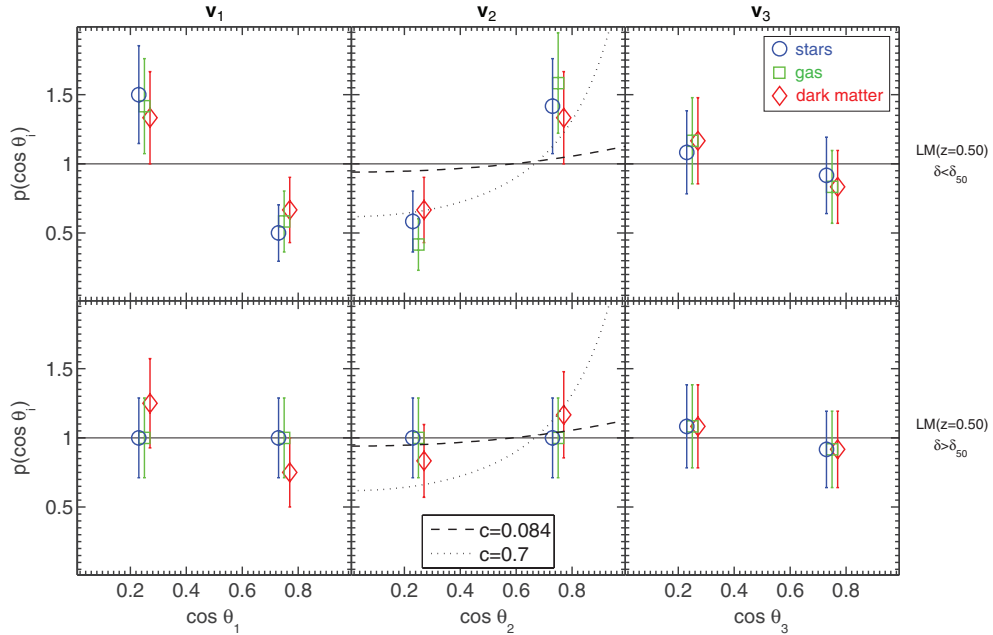

Figure 13. Same as Fig. 12, but for the low-mass (LM) samples at $z = 0.5$, split in low (top) and high (bottom) environmental density.

These results strongly suggest that low-mass galaxies are initially aligned with the intermediate principal axis, as predicted by tidal torque theory, and that this alignment is subsequently destroyed, possibly by environmental effects. Since the alignment with the third principal axis increases during this process, it is plausible that anisotropic galaxy mergers in the filaments or the galaxy's motion along the filament and associated ram-pressure effects or a tidal influence on the gas flow accreting on to the galaxy (see also Hahn et al. 2009) reorient the angular momentum. A first analysis of correlations of the galaxies' mass accretion rates (as a proxy for mergers) and ram pressure with alignment strength did not lead to conclusive results.
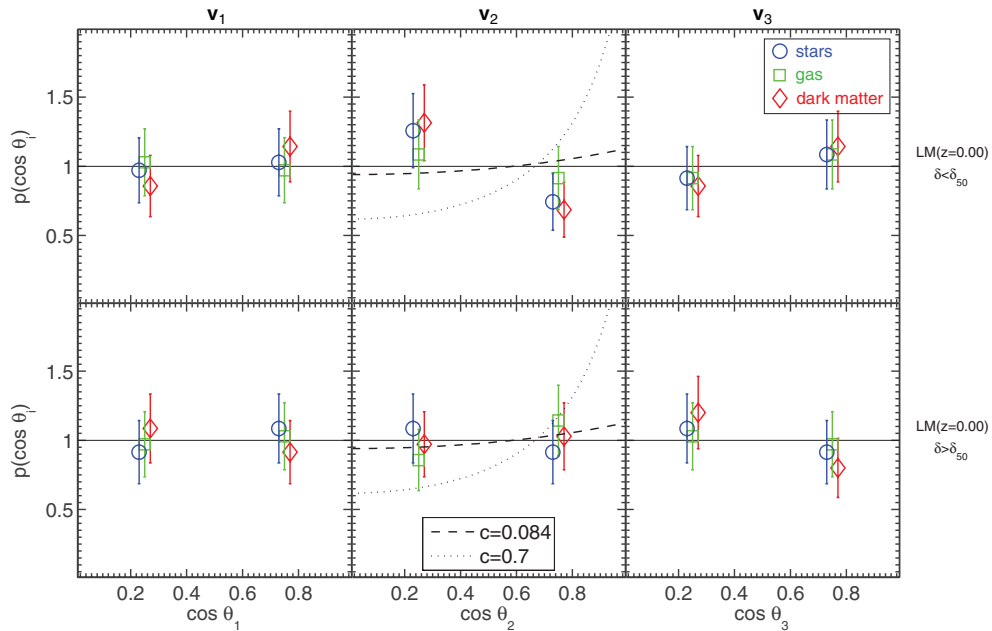
Figure 14. Same as Fig. 12 but for the low mass (LM) samples at $z = 0$, split in low (top) and high (bottom) environmental density.
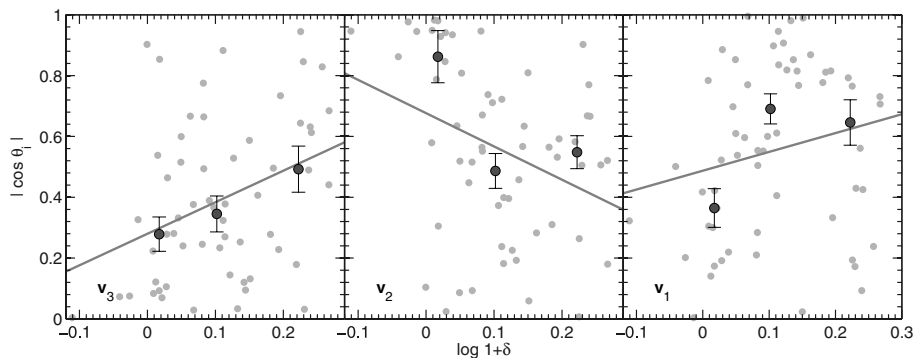

Figure 15. Cosine of the alignment angle of the stellar angular momentum with the three principal axes of the tidal field for all galaxies in the LM sample at $z = 1$ as a function of environmental density determined on scales of physical $2\,h^{-1}$ Mpc. Light grey points indicate the data, dark grey points show binned median values with error bars representing the uncertainty on the median. The lines represent linear least-square fits to the data.

Since tidal torque theory predicts that angular momentum is generated most efficiently at turnaround, it is also plausible that the galaxy's motion simply leads to a decorrelation of the tidal field it resides in at later times from that it experienced at turnaround. Galaxies in higher density regions are likely to have moved further. Specifically, the low-mass galaxies at $z = 1$ have moved from their Lagrangian position (i.e. their centre of mass position in the initial conditions of the simulation) on average $3.3 \pm 1.2\,h^{-1}$ Mpc, comoving, when they reside in regions with $\delta < \delta_{50}$, while the overdense sample shows a mean displacement of $3.9 \pm 1.2\,h^{-1}$ Mpc. We find correlation coefficients between displacement and θ_2 of -0.25. Given that there is no ambiguity in smoothing scale when using the displacements, it is to be expected that this correlation coefficient should be much larger if decorrelation were the only reason for the deviation from tidal-torque prediction for the high-density sample.

Given the inconclusive evidence at this stage, we postpone a thorough investigation of the origin of the observed density dependence to future work.

5 COMPARISON WITH OBSERVATIONS

Most observational results for the alignments of central galaxies exist for elliptical galaxies. Early studies found an alignment of brightest cluster galaxies with the shape of the cluster itself (e.g. Binggeli 1982). More recently, the alignment of LRGs has been detected at high significance in the SDSS (Mandelbaum et al. 2006; Hirata et al. 2007). These LRGs show radial alignment with their surrounding density peaks. These observational detections of elliptical galaxy alignment are consistent with theoretical studies that demonstrate that they form through anisotropic mergers along the filaments at whose nodes they will eventually reside (West 1989; Dubinski 1998). Our results indicate that the spin of the most massive disc galaxies in our samples show a preference for alignment with the third principal axis of the tidal field which is parallel to the overall direction of the filaments (cf. Figs 9–11). This thus corresponds to a radial anti-alignment of the disc shape with the filament. Since we however excluded the scales of galaxy groups from our simulations, we can only speculate on their alignment properties. It

is none the less perfectly consistent with observational results that the anti-aligned disc galaxies will merge along the massive filament with the merger remnant then being aligned with the filament since the orbital angular momentum of a major merger will outweigh the contribution from the spin angular momentum of the contributing disc galaxies (see also Dubinski 1998). Our result could also explain why the alignment signal of massive galaxies seen by Mandelbaum et al. (2006) and Hirata et al. (2007) decays so rapidly when less luminous galaxies are considered and thus the fraction of massive disc galaxies increases.

For lower mass disc galaxies, the observational findings are however less conclusive. Both Mandelbaum et al. (2006) and Hirata et al. (2007) detect no alignment for $L < L_*$ galaxies in SDSS. On the other hand, Lee & Erdogdu (2007) claim a detection of an alignment of 2MASS galaxies with the intermediate principal axis of the reconstructed tidal field. Such an alignment with the intermediate axis is consistent with an alignment of galaxy rotation axes with the shells around cosmic voids. The detection of such an alignment of disc galaxies around voids has been claimed by Trujillo, Carretero & Patiri (2006) in the Two-Degree Field Galaxy Redshift Survey (2dFGRS) and the SDSS. Their analysis was recently repeated by Slosar & White (2009) on the SDSS DR6 who however cannot reproduce the Trujillo et al. (2006) result. The Slosar & White (2009) analysis extends out to a redshift of $\lesssim 0.18$. The strong density dependence of disc galaxy alignment that we found in our analysis is likely to impact these analyses of volume limited galaxy samples. We thus believe that our results are consistent with their non-detection. It is also plausible that the alignment is weaker at low redshifts.

6 SUMMARY AND CONCLUSIONS

We have used a cosmological hydrodynamic simulation of galaxy formation in a large-scale filament to investigate: (1) the orientations of the angular momentum of the stellar and gaseous disc of central galaxies, as well as the inner part of their DM halo with respect to the total angular momentum of the host halo and (2) the orientations of their angular momentum with the surrounding large-scale structure by computing scale-dependent alignments with the tidal field eigenvectors.

The simulation provides us with a sample of ~ 100 disc galaxies at $380\,h^{-1}$pc resolution down to $z = 0$, spanning halo masses between 10^{11} and $10^{13}\,h^{-1}\,{\rm M_{\odot}}$ and stellar masses between 7.5×10^{9} and $8 \times 10^{11}\,h^{-1}\,{\rm M_{\odot}}$. We focus this first analysis on the three simulation snapshots at redshifts 0, 0.5 and 1. We split our sample of galaxies into low-mass galaxies, which are those with a halo mass below the cold accretion limit of $\sim 4 \times 10^{11}\,h^{-1}\,{\rm M_{\odot}}$, and high-mass galaxies above this limit. At $z = 0$, we consider an additional medium mass bin bridging the gap between the cold accretion limit and the non-linear mass scale of $\sim 2 \times 10^{12}\,h^{-1}\,{\rm M_{\odot}}$. Our main results are summarized as follows.

(i) There is an almost perfect alignment at a median of $\sim 18°$ of the stellar, gaseous and inner DM angular momenta at low redshifts. At $z = 1$, there is a slightly weaker alignment at $\sim 36°$ of the stellar and gaseous spins with the DM spin, likely due to the higher fraction of unrelaxed galaxies at that epoch. We do not find any dependence of this alignment signal on environmental density or on halo mass or on stellar mass.

(ii) The distribution of angles between the spin of the central galaxy and the entire host halo is significantly broader, the corresponding median angles larger. We find a median angle of $\sim 50°$ between both the stellar and the gas disc and the total halo angular

momentum at $z = 0$. This median angle decreases slightly at higher redshifts to a median of $\sim 46°$ at $z = 1$. The spin of the inner DM halo is slightly stronger aligned with the total halo. We find a median of ~ 45 degrees at $z = 0$ and $\sim 34°$ at $z = 1$. Again, there is no dependence of this alignment signal on stellar or on halo mass or on environmental density.

(iii) Low-mass galaxies in low-density regions are aligned with the intermediate axis of the large-scale tidal field tensor, peaking on scales of physical $2\,h^{-1}$ Mpc (i.e. $4\,h^{-1}$ Mpc comoving) at $z = 1$ with very high significance. Such an alignment is consistent with the predictions from linear tidal torque theory.

(iv) In density regions above the median overdensity, on scales of physical $2\,h^{-1}$ Mpc, we find however no evidence for alignment of the low-mass galaxies with the intermediate principal axis of the tidal field – at any redshift since $z = 1$. Instead, we find alignment with the first principal axis at $z = 1$, which disappears at later epochs.

(v) We find a strong and significant correlation between environmental density and the degree of alignment with the intermediate axis at $z = 1$. Low-mass galaxies gradually misalign with the intermediate principal axis of the tidal field with increasing environmental density. A possible origin of this effect could be either torques exerted by ram pressure when the galaxies enter in a high-pressure environment, a change in accretion/merger rates in these regions, a gradual decorrelation from the tidal field at formation due to the galaxy's motion in dense regions or a combination of these effects. We will quantitatively investigate this issue in a future study.

(vi) The alignment with the intermediate principal axis of low-mass galaxies in low-density regions weakens with decreasing redshift. The interpretation of this result is not straightforward, as low-mass galaxies show some spurious alignment with the AMR mesh at low redshifts. It is important to stress however that we have evidence, from the analysis of the $z = 1$ and 0.5 snapshots, that non-linear effects do weaken the correlation, raising the question as to whether the absence of alignment at $z = 0$ is a spurious effect due to numerical effects in our simulations or rather an important physical effect. Simulations are planned which are better tailored to establish whether the alignment with the intermediate axis persists in low-density regions down to $z = 0$. Simulations of isolated galaxies hint at the possibility that an alignment signal could persist down to $z = 0$ (Navarro et al. 2004).

(vii) Within the caveats of a limited statistical significance, due to small number statistics, an important trend is unveiled, for the most massive disc galaxies at all redshifts to be aligned with the third principal axis of the tidal field (pointing along the filaments).

Summarizing, low-mass galaxies with halo mass below $4 \times 10^{11}\,h^{-1}$ Mpc are likely to show strong alignment with the intermediate principal axis of the tidal field at redshifts relevant for weak lensing studies. This alignment is significantly weakened in regions of high environmental density, likely due to non-linear effects. We are studying the implications of such alignments for weak lensing experiments such as the European Space Agency (ESA) mission Euclid, under study for launch before the end of the decade to start the quest to constrain the nature of dark energy.

ACKNOWLEDGMENTS

REFERENCES

Agustsson I., Brainerd T. G., 2006a, ApJ, 644, L25

Agustsson I., Brainerd T. G., 2006b, ApJ, 650, 550

Aragón-Calvo M. A., van de Weygaert R., Jones B. J. T., van der Hulst J. M., 2007, ApJ, 655, L5

Azzaro M., Patiri S. G., Prada F., Zentner A. R., 2007, MNRAS, 376, L43

Bailin J., Steinmetz M., 2005, ApJ, 627, 647

Bailin J. et al., 2005, ApJ, 627, L17

Bailin J., Power C., Norberg P., Zaritsky D., Gibson B. K., 2008, MNRAS, 390, 1133

Bett P., Eke V., Frenk C. S., Jenkins A., Okamoto T., 2010, MNRAS, 404, 1137

Binggeli B., 1982, A&A, 107, 338

Birnboim Y., Dekel A., 2003, MNRAS, 345, 349

Bond J. R., Kofman L., Pogosyan D., 1996, Nat, 380, 603

Brunino R., Trujillo I., Pearce F. R., Thomas P. A., 2007, MNRAS, 375, 184

Bryan G. L., Norman M. L., 1998, ApJ, 495, 80

Catelan P., Kamionkowski M., Blandford R. D., 2001, MNRAS, 320, L7

Ciotti L., Dutta S. N., 1994, MNRAS, 270, 390

Ciotti L., Giampieri G., 1998, Celest. Mech., 68, 313

Colless M., Dalton G., Maddox the 2dF collaboration 2001, MNRAS, 328, 1039

Croft R. A. C., Di Matteo T., Springel V., Hernquist L., 2009, MNRAS, 400, 43

Cuesta A. J., Betancort-Rijo J. E., Gottlöber S., Patiri S. G., Yepes G., Prada F., 2008, MNRAS, 385, 867

Dekel A., Birnboim Y., 2006, MNRAS, 368, 2

Dubinski J., 1998, ApJ, 502, 141

Dubois Y., Teyssier R., 2008, A&A, 477, 79

Fakhouri O., Ma C.-P., 2009, MNRAS, 394, 1825

Faltenbacher A., Li C., Mao S., van den Bosch F. C., Yang X., Jing Y. P., Pasquali A., Mo H. J., 2007, ApJ, 662, L71

Faltenbacher A., Jing Y. P., Li C., Mao S., Mo H. J., Pasquali A., van den Bosch F. C., 2008, ApJ, 675, 146

Faltenbacher A., Li C., White S. D. M., Jing Y.-P., Shu-DeMao Wang J., 2009, Res. Astron. Astrophys., 9, 41

Hahn O., Porciani C., Carollo C. M., Dekel A., 2007a, MNRAS, 375, 489

Hahn O., Carollo C. M., Porciani C., Dekel A., 2007b, MNRAS, 381, 41

Hahn O., Porciani C., Dekel A., Carollo C. M., 2009, MNRAS, 398, 1742

Heymans C., White M., Heavens A., Vale C., van Waerbeke L., 2006, MNRAS, 371, 750

Hirata C. M., Seljak U., 2004, Phys. Rev. D, 70, 063526

Hirata C. M., Mandelbaum R., Ishak M., Seljak U., Nichol R., Pimbblet K. A., Ross N. P., Wake D., 2007, MNRAS, 381, 1197

Hockney R. W., Eastwood J. W., 1981, Computer Simulation using Particles. McGraw-Hill, New York

Hoshen J., Kopelman R., 1976, Phys. Rev. B, 14, 3438

Joachimi B., Schneider P., 2008, A&A, 488, 829

Kereš D., Katz N., Weinberg D. H., Davé R., 2005, MNRAS, 363, 2

King L. J., 2005, A&A, 441, 47

Knebe A., Draganova N., Power C., Yepes G., Hoffman Y., Gottlöber S., Gibson B. K., 2008, MNRAS, 386, L52

Komatsu E., Dunkley J., Nolta M. R., Bennett C. L., the WMAP collaboration, 2009, ApJS, 180, 330

Lee J., Erdogdu P., 2007, ApJ, 671, 1248

Lee J., Hahn O., Porciani C., 2009a, ApJ, 705, 1469

Lee J., Hahn O., Porciani C., 2009b, ApJ, 707, 761

Mandelbaum R., Hirata C. M., Ishak M., Seljak U., Brinkmann J., 2006, MNRAS, 367, 611

May A., James R. A., 1984, MNRAS, 206, 691

Navarro J. F., Abadi M. G., Steinmetz M., 2004, ApJ, 613, L41

Ocvirk P., Pichon C., Teyssier R., 2008, MNRAS, 390, 1326

Okumura T., Jing Y. P., Li C., 2009, ApJ, 694, 214

Patiri S. G., Cuesta A. J., Prada F., Betancourt-Rijo J., Klypin A., 2006, ApJ, 652, L75

Paz D. J., Stasyszyn F., Padilla N. D., 2008, MNRAS, 389, 1127

Peebles P. J. E., 1969, ApJ, 155, 393

Pereira M. J., Bryan G. L., Gill S. P. D., 2008, ApJ, 672, 825

Porciani C., Dekel A., Hoffman Y., 2002, MNRAS, 332, 325

Rasera Y., Teyssier R., 2006, A&A, 445, 1

Schäfer B. M., 2009, Int. J. Mod. Phys. D, 18, 173

Schneider M. D., Bridle S., 2010, MNRAS, 402, 2127

Shandarin S. F., Zeldovich Y. B., 1989, Rev. Mod. Phys., 61, 185

Sharma S., Steinmetz M., 2005, ApJ, 628, 21

Slosar A., White M., 2009, J. Cosmol. Astropart. Phys., 6, 9

Tegmark M., Blanton M. R., Strauss M. A., The SDSS Collaboration, 2004, ApJ, 606, 702

Teyssier R., 2002, A&A, 385, 337

Trujillo I., Carretero C., Patiri S. G., 2006, ApJ, 640, L111

van den Bosch F. C., Abel T., Croft R. A. C., Hernquist L., White S. D. M., 2002, ApJ, 576, 21

West M. J., 1989, ApJ, 347, 610

White S. D. M., 1984, ApJ, 286, 38

Yang X., van den Bosch F. C., Mo H. J., Mao S., Kang X., Weinmann S. M., Guo Y., Jing Y. P., 2006, MNRAS, 369, 1293

Zel'Dovich Y. B., 1970, A&A, 5, 84

Zentner A., Kravtsov A. V., Gnedin O. Y., Klypin A. A., 2005, ApJ, 629, 219

APPENDIX A: ASSESSMENT OF NUMERICAL EFFECTS ON GALAXY ORIENTATIONS

A1 The lower resolution simulation

We also performed a simulation of the filament described in Section 2.1 at identical mass resolution but with a lower maximum refinement level so that the maximum spatial resolution is $0.76\,h^{-1}$ kpc at all times, a factor of 2 lower than the simulation used in our analysis. We analysed this simulation in an identical way as the higher resolution one and quantify the differences in what follows in order to determine the numerical reliability of our results. The lower spatial resolution should especially demonstrate

Table A1. Same as Table 2, but for the simulation with two-times lower spatial resolution.

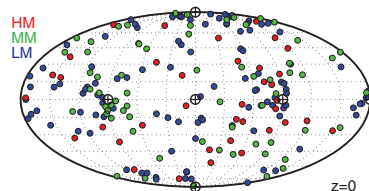| Median	$z = 0$
$\cos\theta_{S,G}$	$0.988^{+0.001}_{-0.002}$
$\cos\theta_{S,DM}$	$0.953^{+0.002}_{-0.019}$
$\cos\theta_{G,DM}$	$0.924^{+0.004}_{-0.022}$
$\cos\theta_{S,tot}$	$0.627^{+0.018}_{-0.055}$
$\cos\theta_{G,tot}$	$0.594^{+0.013}_{-0.052}$
$\cos\theta_{DM,tot}$	$0.745^{+0.013}_{-0.048}$

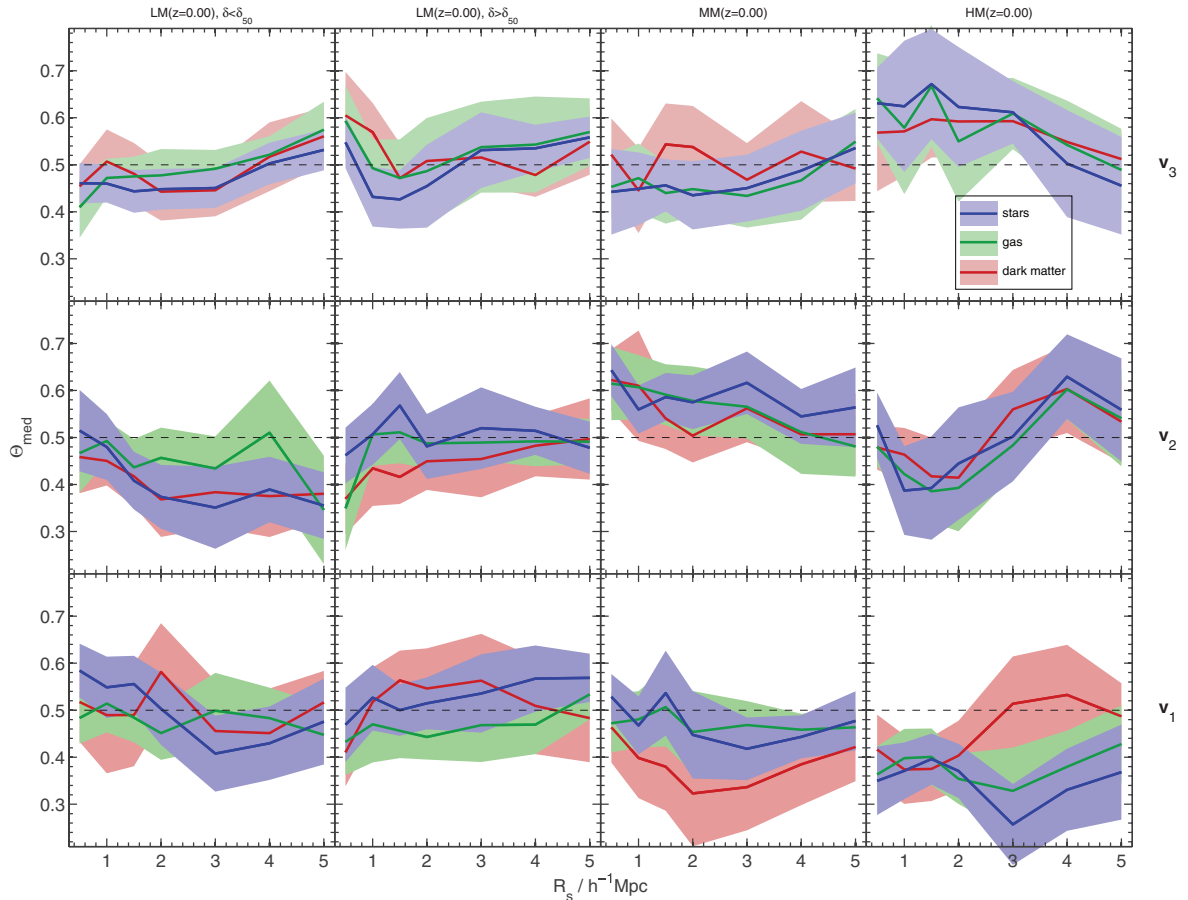**Figure A1.** Same as Fig. 8, but for the low-resolution run at $z = 0$.

Figure A2. Same as Fig. 9, but for the simulation with two-times lower spatial resolution at redshift $z = 0$. The corresponding results for the high-resolution run are shown in Fig. 11.

whether the galaxy orientations are affected by force anisotropy at the resolution level.

We decide to keep the mass samples identical to those in the previous sections so that galaxies on average contain eight times less star particles (and thus more than 3000), but an equal amount of DM particles. We compare our results at $z = 0$ as spurious grid alignment effects are expected to be strongest in the dark energy dominated period where the merger rates decline substantially and the galaxies thus could potentially relax to the grid. The low-resolution simulation contains slightly more galaxies since additional refinement, cooling and star formation were not restricted to not contain the massive groups. These group galaxies are however not included in our comparison as we restrict ourselves to the central galaxies of haloes that are resolved in both simulations.

A2 Angular momentum correlations in the galaxy and with the host halo

In Table A1, we give the median angles between the stellar, gas and DM component within the galaxies and with the total halo angular momentum at $z = 0$ for the low-resolution run. Comparing these angles with those of the high-resolution run in Table 2, we find that the median alignment angles obtained at lower spatial resolution are marginally larger, the corresponding vectors thus less aligned. Given the width of the distributions, the results can however be considered consistent at high significance.

A3 Isotropy of the galaxy spins

In Fig. A1, we show the orientations of stellar angular momentum vectors for the low-resolution simulation. This should be compared with the corresponding Fig. 8 for the high-resolution run. Visually, we see a stronger clustering of spin vectors around the Cartesian mesh basis vectors than for the high-resolution run. Spurious grid alignment is thus present at $z = 0$ in both simulations to some degree.

A4 Alignments with the tidal field

In Fig. A2, we show the scale dependence of the alignment between the galaxy stellar, gas and DM angular momentum and the three eigenvectors of the tidal field for the low-resolution run. These results should be compared with results for the high-resolution simulation given in Fig. 11. We find that the results are perfectly consistent for all samples except the low-density low-mass bin where we find a slightly stronger anti-alignment with the intermediate principal axis of the tidal field in the low-resolution run. Also, the weak anti-alignment with the third principal axis is not seen in the high-resolution run. It is likely that this difference for low-mass galaxies in low-density regions is due to the anisotropy induced by the Cartesian mesh which is expected to be stronger for the low-resolution run. We conclude that the resolution of our high resolution run is still insufficient for galaxy orientations to be not

affected by spurious grid relaxation in low-density regions at low redshifts. It is thus not clear whether the alignment of spins with the intermediate axis that we find at higher redshifts would persist in low-density environments also down to $z = 0$ in the absence of numerical effects. This question has to be addressed with even higher resolution simulations than the ones we used in our analysis. The results of Navarro et al. (2004), who find a survival of align-ment with the intermediate axis for the four isolated galaxies they simulated, is however indicative that such alignment should persist to some degree.

This paper has been typeset from a TeX/LaTeX file prepared by the author.